


Article

Ab Initio Phase Diagram of Chromium to 2.5 TPa

Samuel R. Baty ^{1,†}, Leonid Burakovsky ^{1,*}, Darby J. Luscher ^{1,†}, Sky K. Sjue ^{1,†} and Daniel Errandonea ^{2,†}¹ Los Alamos National Laboratory, Los Alamos, NM 87545, USA² Departamento de Física Aplicada-ICMUV, MALTA Consolider Team, Universidad de Valencia, Edificio de Investigación, C/Dr. Moliner 50, Burjassot, 46100 Valencia, Spain

* Correspondence: burakov@lanl.gov; Tel.: +1-505-667-5222

† These authors contributed equally to this work.

Abstract: Chromium possesses remarkable physical properties such as hardness and corrosion resistance. Chromium is also a very important geophysical material as it is assumed that lighter Cr isotopes were dissolved in the Earth's molten core during the planet's formation, which makes Cr one of the main constituents of the Earth's core. Unfortunately, Cr has remained one of the least studied 3d transition metals. In a very recent combined experimental and theoretical study (Anzellini et al., Scientific Reports, 2022), the equation of state and melting curve of chromium were studied to 150 GPa, and it was determined that the ambient body-centered cubic (bcc) phase of crystalline Cr remains stable in the whole pressure range considered. However, the importance of the knowledge of the physical properties of Cr, specifically its phase diagram, necessitates further study of Cr to higher pressure. In this work, using a suite of ab initio quantum molecular dynamics (QMD) simulations based on the Z methodology which combines both direct Z method for the simulation of melting curves and inverse Z method for the calculation of solid–solid phase transition boundaries, we obtain the theoretical phase diagram of Cr to 2.5 TPa. We calculate the melting curves of the two solid phases that are present on its phase diagram, namely, the lower-pressure bcc and the higher-pressure hexagonal close-packed (hcp) ones, and obtain the equation for the bcc-hcp solid–solid phase transition boundary. We also obtain the thermal equations of state of both bcc-Cr and hcp-Cr, which are in excellent agreement with both experimental data and QMD simulations. We argue that 2180 K as the value of the ambient melting point of Cr which is offered by several public web resources (“Wikipedia,” “WebElements,” “It’s Elemental,” etc.) is most likely incorrect and should be replaced with 2135 K, found in most experimental studies as well as in the present theoretical work.

Keywords: quantum molecular dynamics; melting curve; solid–solid phase transition boundary; equation of state; multi-phase materials



Citation: Baty, S.R.; Burakovsky, L.; Luscher, D.J.; Sjue, S.K.; Errandonea, D. Ab Initio Phase Diagram of Chromium to 2.5 TPa. *Appl. Sci.* **2022**, *12*, 7844. <https://doi.org/10.3390/app12157844>

Academic Editor: Antonio Miotello

Received: 16 June 2022

Accepted: 28 July 2022

Published: 4 August 2022

Publisher's Note: MDPI stays neutral with regard to jurisdictional claims in published maps and institutional affiliations.



Copyright: © 2022 by the authors. Licensee MDPI, Basel, Switzerland. This article is an open access article distributed under the terms and conditions of the Creative Commons Attribution (CC BY) license (<https://creativecommons.org/licenses/by/4.0/>).

1. Introduction

Chromium is the fourth 3d transition metal found in the periodic table. It is the first element known to violate one of the aufbau (building-up) principles, specifically the Madelung energy ordering rule, as its electron configuration is [Ar]3d⁵4s¹ rather than [Ar]3d⁴4s² predicted by this rule. Chromium is extremely hard, being the third hardest element behind carbon (diamond) and boron. Chromium is also valued for its high corrosion resistance which finds its application in stainless steel production. Chromium-based catalysts are widely used for industrial production of polyethylene and 1-hexene.

Chromium is also an important geophysical material. It is the Earth's 10th most abundant element, behind iron, oxygen, silicon, magnesium, sulfur, etc. Comparison of the concentrations of elements found in the meteorites that are of the same age as the Earth (4.5 billion years) to those found in the Earth's crust sheds light on how the Earth was formed. It appears that these meteorites contain more chromium than the Earth [1], which constitutes the so-called missing chromium problem. The resolution of this problem was

found in [1]. Using Cr isotope measurements from both the meteorites and the Earth's crust, it was shown [1] that lighter Cr isotopes sank into the Earth's core during the planet's formation. In addition, first-principles-based computer simulations revealed [1] that this process occurred in the early stages of the Earth's formation when smaller bodies were coalescing to form the contemporary Earth.

Thus, the knowledge of the physical properties of chromium is very important for materials science and condensed matter physics as well as for geophysics, since being one of the main constituents of the Earth's core, its physical properties are directly related to the Earth's thermal history. Unfortunately, chromium has remained one of the least studied 3d transition metals. Most of the information on its physical properties is available at low pressure (P) only. Its crystal structure at ambient conditions is body-centered cubic (bcc). With decreasing temperature (T), bcc is modified by two first-order phase transitions: to antiferromagnetic (AF) phase with orthorhombically distorted bcc at the Néel T (T_N) of 311 K, and to AF phase with tetragonally distorted bcc at the spin-flip T of 123 K [2]. In both phases, the bcc distortions are too small to be detected by X-ray diffraction. The physical reasons for the ground state of Cr being AF have been discussed in several papers; see, e.g., Ref. [3], which provides arguments for bcc-Fe being ferromagnetic (FM) but both bcc-Mn and bcc-Cr being AF. Above 311 K, Cr is paramagnetic (PM).

With increasing P , chromium is expected to exhibit a polymorphism, similar to both molybdenum and tungsten, its partners in Period 6B of the periodic table (PT), the high- P crystal structure of which is double-hexagonal-close-packed (double-hcp, or dhcp) [4]. Indeed, a solid–solid (s-s) phase transition into hcp is predicted theoretically for Cr, but the values of the transition P that can be found in the literature span an interval of 7–12.5 Mbar [5]. The melting curve of chromium was measured experimentally in [6], along with that of vanadium and other transition metals. It appeared to be the so-called “low” melting curve which virtually flattens out at $P \sim 1$ Mbar and for which the value of T at the melting point (T_m) on the shock Hugoniot is much lower than that extracted from the shock compression data. Moreover, it appeared to virtually coincide with the melting curve of V. The latter was very thoroughly re-measured recently [7] and shown to be actually the so-called “high” melting curve for which the value of the shock T_m is in agreement with the shock data. Thus, the melting curve of Cr of Ref. [6] is most likely erroneous, just like that of V, and therefore needs to be corrected via being carefully re-measured experimentally and/or calculated theoretically.

Even the value of the ambient T_m of Cr is ambiguous. $T_m = 2136$ K can be found in Young's book [8]. Very accurate experimental measurements of Refs. [9,10] give, respectively, $T_m = 2136$ and 2131 ± 5 K. According to [11], the experimental values of the ambient T_m of Cr that can be found in the literature span an interval of 2085(10)–2180(20), i.e., $\sim 2130 \pm 50$. The value $T_m = 2180$ K which is offered by several public web resources (“Wikipedia,” “WebElements,” “It's Elemental,” etc.) comes from Ref. [12] and is most likely incorrect. Specifically, in [12] this value was assessed, along with that of the melting enthalpy ΔH_m (latent heat of melting), based on some literature data. The latter turns out to be $\Delta H_m = 21$ kJ/mol [12]. The value of ΔH_m from the experiment of Ref. [9] is 29,674(574) J/mol, and that calculated in [13] based on the accurate literature data is $\approx 28,000$ J/mol. Thus, $\Delta H_m \sim (29 \pm 1)$ kJ/mol, so that the assessment of Ref. [12] leading to 21 kJ/mol is very likely incorrect, and so is their value of T_m of 2180 K. In the experiment of Ref. [11], Cr melts at T between 2120 and 2150 K, i.e., at 2135 ± 15 K. Our own theoretical results on the melting of Cr discussed below lead to $T_m = 2135$ K.

To address all of the above points of concern related to the phase diagram of chromium, in this work we carry out its extensive theoretical study to a pressure of 2.5 TPa (25 Mbar). This work continues a previous combined experimental and theoretical study of Cr in which its equation of state and melting curve were determined to a pressure of 150 GPa [14]. It is necessitated by the importance of the knowledge of the physical properties of Cr, specifically its phase diagram, to higher P .

2. Methods

Our theoretical calculations of the equation of state and melting curve of Cr are based on density-functional theory (DFT) with the projector-augmented-wave (PAW) [15] implementation and the generalized gradient approximation (GGA) for exchange-correlation energy, in the form known as Perdew-Burke-Ernzerhof (PBE) [16]. For these calculations, Vienna Ab initio Simulation Package (VASP) [17] was used. The reason for choosing GGA instead of another implementation of DFT, namely, local density approximation (LDA), is that it has been known that LDA does not accurately describe the properties of 3d transition metals, specifically chromium, for which its predictions are in drastic disagreement with experiment [18,19], and iron, for which it produces a wrong ground state: AF or nonmagnetic (NM) bcc [20,21] or NM-hcp [22–24] instead of FM-bcc. LDA also fails in assessing the strength of the magnetovolume effect. On the other hand, GGA correctly predicts the structural and magnetic phase diagrams [25].

Cr was modeled using the core-valence representation [$^{12}\text{Mg}]\text{3p}^6\text{3d}^5\text{4s}^1$, i.e., we assign the 12 outermost electrons to the valence. The valence electrons are represented with a plane-wave basis set with a cutoff energy of 350 eV, while the core electrons are represented by projector augmented-wave (PAW) pseudopotential (PP). The core radius (RCUT) for this PP is 2.3 a.u., or 1.22 Å. Since numerical errors in the VASP calculations remain almost negligible until the nearest neighbor distance reaches $2 \times \text{RCUT} / (1.25 \pm 0.05)$, with this PP one can study systems with densities up to $\sim 22.5 \text{ g/cm}^3$, at least at low T . With our EOS of Cr, this corresponds to $P \sim 2.5 \text{ TPa}$.

Cold ($T = 0$) EOSs and enthalpies were calculated using unit cells with very dense k -point meshes for high accuracy. Specifically, for bcc-Cr and hcp-Cr, k -point meshes of $50 \times 50 \times 50$ and $50 \times 50 \times 30$ were used. In all the non-cubic cases, we first relaxed the structure to determine its unit cell parameters at each volume. The AF bcc-Cr was studied in the framework of fully unconstrained noncollinear magnetism developed in Ref. [25]. In all the calculations including the simulations of the bcc-Cr and hcp-Cr melting curves and the inverse-Z solidification simulations discussed below, periodic boundary conditions were used.

The theoretical melting curve of chromium (as the combination of those of both bcc-Cr and hcp-Cr) was calculated via ab initio quantum molecular dynamics (QMD) simulations using the Z method implemented with VASP, which is described in detail in Refs. [26–28]. We used a 432-atom ($6 \times 6 \times 6$) bcc-Cr supercell and a 392-atom ($7 \times 7 \times 4$) hcp-Cr supercell with a single Γ -point in each case. This was sufficient to ensure full energy convergence (to $\lesssim 1 \text{ meV/atom}$) which was checked for each simulation. We obtained a total of 12 melting points (six for bcc-Cr and six for hcp-Cr), and for each of them, 10 NVE (fixed total number of atoms N , system volume V , and total energy E ; V corresponds to one of the six densities from Table 1) runs of 10,000–20,000 time steps of 1.0 fs each. For bcc-Cr, increments of the initial T were 125 K for the 1st, 250 K for the 2nd, 375 K for the 3rd and 4th, and 500 K for the 5th and 6th T_m . For hcp-Cr, those increments were also 125 K for the 1st, 250 K for the 2nd, 375 K for the 3rd, 500 K for the 4th, and 625 K for the 5th and 6th T_m . The corresponding error in T_m is half of the increment of the initial T [28] so that it does not exceed $\sim 4\%$ for each of the six bcc-Cr T_m s and $\sim 5\%$ for each of the six hcp-Cr T_m s. The errors in P are negligibly small: $\lesssim 0.5 \text{ GPa}$ for the first point, and 1–2 GPa for the remaining five in either case. Hence, our melting results on both bcc-Cr and hcp-Cr are very accurate.

Examples of our Z method melting simulations can be found in Ref. [14] (Figures 3 and 4 of [14]).

For inverse-Z solidification simulations described in detail in Ref. [27], we used a computational cell of 512 atoms prepared by melting a $8 \times 8 \times 8$ solid simple cubic (sc) supercell, which would eliminate any bias towards solidification into bcc or any other solid structure (fcc, hcp, dhcp, etc.). We used sc unit cells of 1.810, 1.770, 1.735 and 1.700 Å; the corresponding densities are (in g/cm^3), respectively, 14.561, 15.570, 16.532 and 17.574, which corresponds to P of $\sim 650, 800, 1000$ and 1200 GPa. We carried out NVT simulations using

the Nosé–Hoover thermostat with a timestep of 1 fs, with the initial T increment of 2500 K. Complete solidification typically required from 15 to 25 ps, or 15,000–25,000 timesteps.

3. Results

3.1. Cold ($T = 0$) Enthalpies of Different Solid Structures of Cr

Our calculated cold enthalpies of three other solid structures of Cr in relation to that of bcc-Cr assumed to be identically zero are shown in Figure 1. We note that the enthalpy of bcc-Cr combines its AF and NM counterparts, below and above ~ 20 GPa, respectively. It is seen that, with increasing P , three other solid structures become thermodynamically more stable than bcc, but it is hcp that does it first, at a pressure of 709.7 GPa. Hence, in contrast to both Mo and W (each having dhcp as a high- P solid structure), in the case of Cr, the s-s phase transition boundary is the bcc-hcp one, and its starting point is $(P, T) \approx (710, 0)$. Pressure as high as this is nowadays achievable in a diamond anvil cell [29]; thus, our prediction can be tested experimentally.

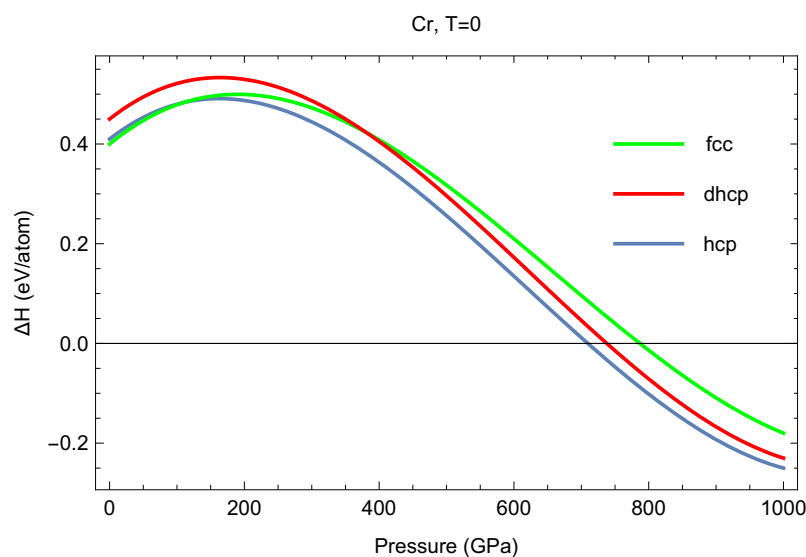


Figure 1. Cold enthalpies of three other solid structures of Cr as a function of P in relation to that of bcc-Cr assumed to be identically zero.

3.2. Equations of State of bcc-Cr and hcp-Cr

The $(P = 0, T = 0)$ ground state corresponds to a bcc-Cr density of 7.229 g/cm^3 (a lattice constant of 2.88 \AA or an atomic volume of 11.944 \AA^3), or a molar volume of 7.193 cm^3 , in excellent agreement with 7.2 cm^3 from experiment [30]. At this density, the NM bcc-Cr is higher in energy by $\sim 20 \text{ meV/atom}$, i.e., the ground state of bcc-Cr is correctly predicted to be AF. However, the calculated magnetic moment per atom (MMA), $\sim 1.1 \mu_B$, is somewhat larger than the experimental $0.62 \mu_B$ [31], which is typical as regards a discrepancy between theory and experiment for this type of theoretical calculation [31,32]. MMA depends almost linearly on the bcc-Cr lattice constant, a : $\mu(a) \approx 1.1 + 14(a - 2.88)$, and turns zero at a density of 7.87 g/cm^3 (or $a \approx 2.8 \text{ \AA}$); the corresponding P is $\sim 22 \text{ GPa}$. This P is higher than $\sim 10 \text{ GPa}$ (or $a \approx 2.84 \text{ \AA}$) where the experimental Néel T turns zero as a function of P (or a) [33] but is consistent with another theoretical work [32] which shows that the calculated MMA is suppressed considerably at a pressure of $\sim 20 \text{ GPa}$. At $P \gtrsim 20 \text{ GPa}$, the EOS of AF bcc-Cr merges into that of NM bcc-Cr, so that the two EOSs become virtually identical. Both AF bcc-Cr below 20 GPa and NM bcc-Cr above 20 GPa combined are described by the third-order Birch–Murnaghan EOS (here ρ stands for density, in g/cm^3 , and B and B' for bulk modulus, in GPa, and its pressure derivative, and the subscript 0 implies $(P = 0, T = 0)$).

$$P(\rho) = \frac{3}{2} B_0 (\eta^{7/3} - \eta^{5/3}) \left[1 + \frac{3}{4} (B'_0 - 4) (\eta^{2/3} - 1) \right], \quad (1)$$

where $\eta = \rho/\rho_0$ and $\rho_0 = 7.229$, $B_0 = 215.2$, $B'_0 = 4.1$. This EOS is expected to be reliable to ~ 2.5 TPa as discussed above. In Figure 2, we compare our theoretical results on the cold EOS of bcc-Cr to the most recent experimental data by Anzellini et al. [14] and to the EOS obtained from the shock Hugoniot data by McQueen et al. [34]. It is clearly seen that agreement between theory and the most recent experiment is excellent.

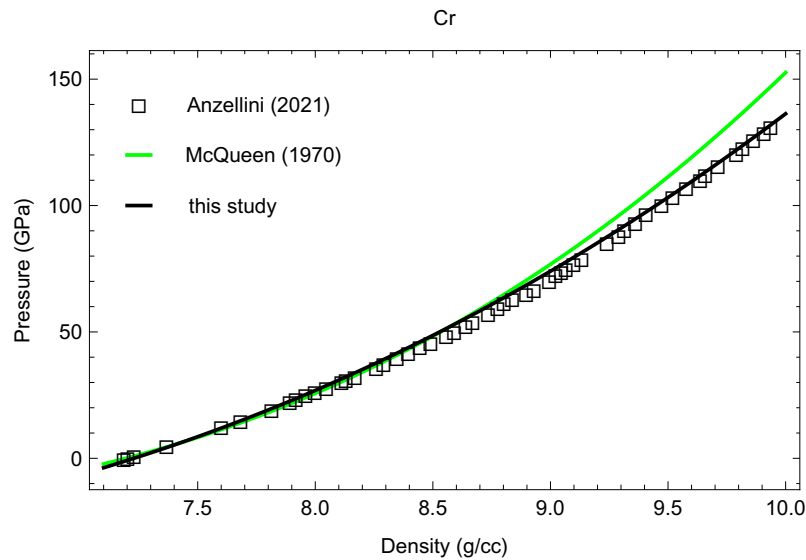


Figure 2. The cold equation of state of bcc-Cr: comparison of our theoretical results to the most recent experimental data (Anzellini, [14]) and the EOS obtained from the shock Hugoniot data (McQueen, [34]).

We note that the above EOS does not explicitly contain PM-Cr. However, we did calculate the EOS of PM bcc-Cr using the GGA + U scheme with spin-orbit coupling developed for the calculation of the properties of paramagnetic materials [35]. Specifically, we used the Dudarev approach [36] in which only the difference $U - J$ is meaningful rather than the values of the two parameters separately. We adopted $U - J = 4.5$ eV from [37]. We found that the EOSs of both PM bcc-Cr and NM bcc-Cr virtually coincide, because the difference in the two values of P at the same density decreases with increasing density, and eventually becomes negligibly small. Furthermore, we calculated two melting points of PM bcc-Cr (the calculation of the melting curve is discussed above). Although the corresponding values of P and T are slightly different from those of NM bcc-Cr having the same densities, these two melting points lie on the melting curve of NM bcc-Cr, Equation (3) below. Thus, the melting curves of both PM-Cr and NM-Cr are virtually identical. Since their EOSs are virtually identical, too, for the purpose of the present study there is no difference in the choice of the structure of bcc-Cr as either paramagnetic or nonmagnetic. For the calculation of the melting curve of Cr presented in what follows, the nonmagnetic structure was chosen.

Cold EOS of hcp-Cr is described by the BM3 form, Equation (1), with

$$\rho_0 = 7.244 \text{ g/cm}^3, \quad B_0 = 198.7 \text{ GPa}, \quad B'_0 = 4.1. \quad (2)$$

The P dependence of the c/a ratio for the lattice constants of the hcp-Cr unit cell is shown in Figure 3. Above 1000 GPa, the hcp-Cr structure is virtually ideal ($c/a = 2\sqrt{2/3} \approx 1.633$). At the transition P of 710 GPa, the two density values predicted by these EOSs are, respectively (in g/cm^3), 14.967 for bcc-Cr and 15.348 for hcp-Cr; hence the bcc-hcp transition corresponds to a small volume change of $\sim 2.5\%$.

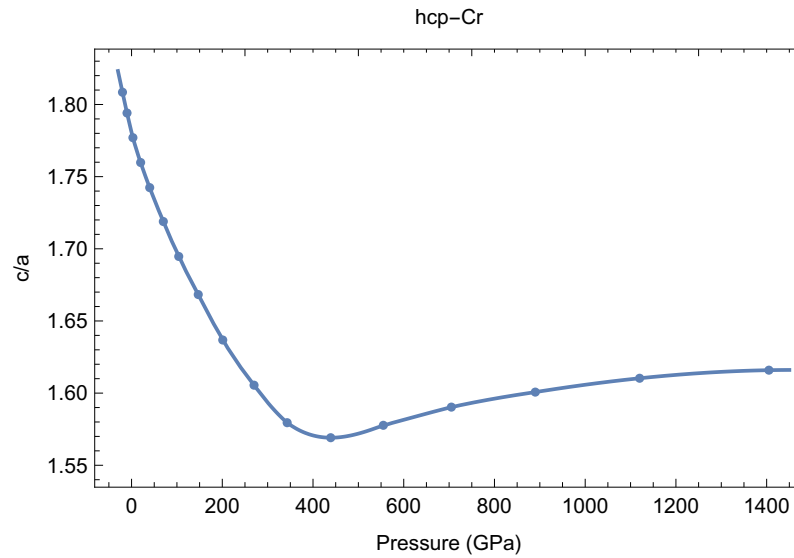


Figure 3. The P -dependence of the c/a ratio for the lattice constants of the hcp-Cr unit cell.

3.3. Ab Initio Melting Curve of bcc-Cr

The six melting points of bcc-Cr that we obtained are listed in Table 1.

Table 1. The six ab initio melting points of bcc-Cr, (P_m , $T_m \pm \Delta T_m$), obtained from the Z method implemented with VASP.

Lattice Constant (Å)	Density (g/cm ³)	P_m (GPa)	T_m (K)	ΔT_m (K)
3.0	6.3957	−5.2	1950	62.5
2.8	7.8665	47.9	3330	125.0
2.65	9.2793	124	4460	187.5
2.5	11.052	266	5840	187.5
2.35	13.306	526	7720	250.0
2.25	15.160	815	9310	250.0

Interpolating between the corresponding six points in Table 1 leads to $T_m = T_m(\rho)$, such that at the experimental ambient melting density of solid Cr of $\rho_S = 6.575 \text{ g/cm}^3$ [10] $T_m = 2134.9 \text{ K}$. Hence, in our simulations the ambient melting point is $\approx 2135 \text{ K}$. Fitting the six melting points in Table 1 by the Simon–Glatzel functional form with $T_m(0) = 2135 \text{ K}$ fixed gives

$$T_m(P) = 2135 \left(1 + \frac{P}{25.7} \right)^{0.42}, \quad (3)$$

which is our theoretical melting curve of bcc-Cr. It is supported by the most recent experimental melting data [14]. Its initial slope, $dT_m(P)/dP|_{P=0}$, is 34.9 K/GPa . Let us compare this value to that given by the Clausius–Clapeyron (CC) formula $dT_m(P)/dP|_{P=0} = T_m(0) \cdot \Delta V_m / \Delta H_m$ using the corresponding experimental input. According to [10], the ambient melting density of liquid Cr is $\rho_L = 6.170 \text{ g/cm}^3$. This, along with $\rho_S = 6.575 \text{ g/cm}^3$, leads to volume change at melt $\Delta V_m = 0.519 \text{ cm}^3/\text{mol}$. According to another set of thermal expansion data on Cr [38], $\rho_L = 6.156 \text{ g/cm}^3$ and $\rho_S = 6.509 \text{ g/cm}^3$, so $\Delta V_m = 0.458 \text{ cm}^3/\text{mol}$. To accommodate both data sets, we take $\Delta V_m = 0.49 \pm 0.03 \text{ cm}^3/\text{mol}$. With the latent heat of melting of $\Delta H_m = 29 \pm 1 \text{ kJ/mol}$ (see above), the CC formula gives $dT_m(P)/dP|_{P=0} = 36.1 \pm 2.5$, which our theoretical value is in good agreement with. Another theoretical value of the initial slope, 33.5 K/GPa [39], is also consistent with the CC formula. We note that the use of $\Delta H_m = 21 \text{ kJ/mol}$ from [12] would result in the value of $dT_m(P)/dP|_{P=0}$ being about 50%

higher and would contradict the experimental data. This strongly suggests that the assessment of Ref. [12] is incorrect, and so is the value of $T_m(0)$ of 2180 K proposed in [12].

3.4. Ab Initio Melting Curve of hcp-Cr

The six melting points of hcp-Cr that we obtained are listed in Table 2.

Table 2. The six ab initio melting points of hcp-Cr, (P_m , $T_m \pm \Delta T_m$), obtained from the Z method implemented with VASP.

a (Å)	c (Å)	Density (g/cm ³)	P_m (GPa)	T_m (K)	ΔT_m (K)
2.6053	4.7355	6.2036	1.7	1270	62.5
2.3593	4.0556	8.8329	129	3710	125.0
2.2125	3.5521	11.468	347	5860	187.5
2.0737	3.2715	14.174	692	8170	250.0
1.9630	3.1422	16.468	1093	10190	312.5
1.8565	2.9999	19.285	1744	12890	312.5

The best fit to these six hcp-Cr points gives the melting curve of hcp-Cr in the Simon–Glatzel form (T_m in K, P in GPa):

$$T_m(P) = 1205 \left(1 + \frac{P}{15.4} \right)^{0.50} . \quad (4)$$

Figures 4 and 5 demonstrate the time evolution of T and P , respectively, in the Z-method runs of the hcp-Cr melting point (P in GPa, T in K) (1093, 10,190), the fifth of the six T_m s in Table 2. They are similar to Figures 3 and 4 of Ref. [14] for the bcc-Cr melting point (124, 4460), the third of the six T_m s in Table 1.

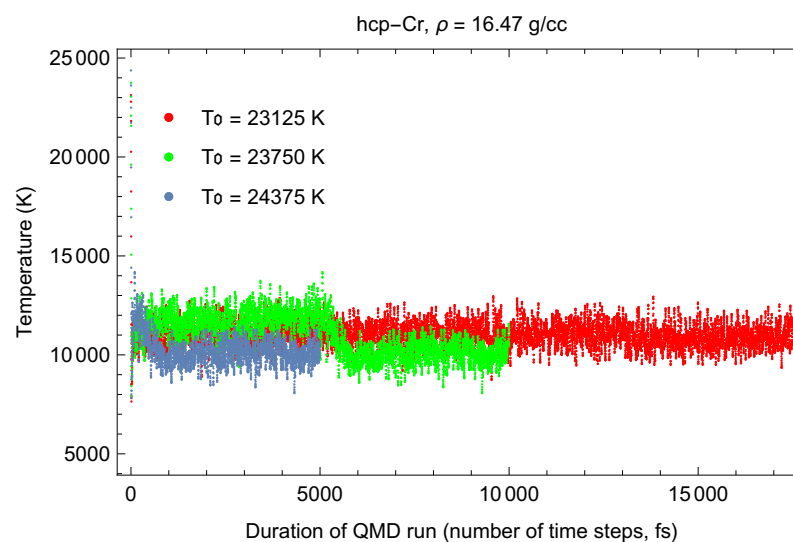


Figure 4. Time evolution of temperature in three QMD runs with initial temperatures (T_0 s) separated by 625 K. The middle run is the melting run during which T decreases from $\sim 12,000$ K for the superheated state to 10,190 K for the liquid at the corresponding melting point.

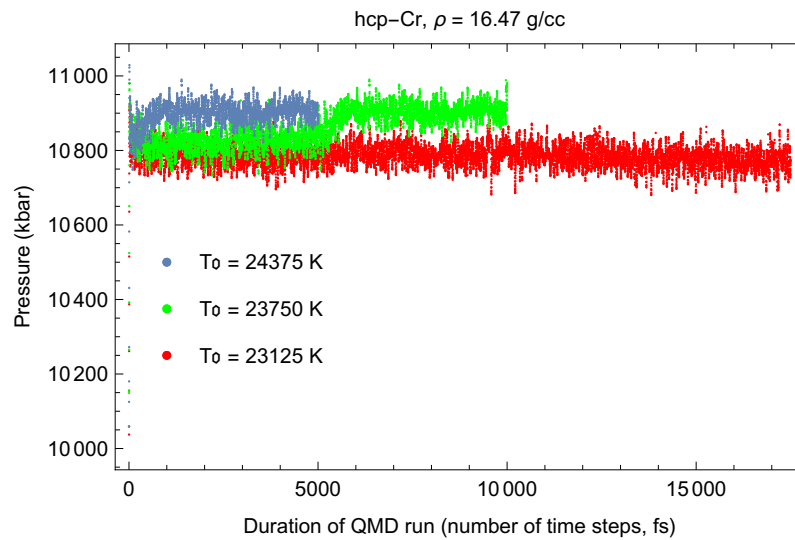


Figure 5. The same as in Figure 4 for the time evolution of pressure (in kbar; 10 kbar = 1 GPa). During melting, P increases from ~ 1080 GPa for the superheated state to 1093 GPa for the liquid at the corresponding melting point.

The other two solid structures that we considered, namely, fcc-Cr and dhcp-Cr, melt below bcc at lower P and below hcp at higher P .

The melting curves of bcc-Cr and hcp-Cr cross each other at (P in GPa, T in K) $(P, T) = (1370.9, 11433)$ which is the bcc-hcp-liquid triple point. The choice of $T(P) = a(710 - P)^b$, $0 < b < 1$ as a functional form for the bcc-hcp solid–solid phase transition boundary leads to:

$$T(P) = 33.1 (P - 710)^{0.90}, \quad (5)$$

which crosses the triple point and lies within the bounds imposed by the solidification simulations using the inverse Z method. We discuss these inverse Z simulations in the following section. Note that the value $b = 0.9$ for Cr is exactly the same as for both of its PT partners Mo and W [4].

Although the rigorous derivation of the thermal equations of state of bcc-Cr and hcp-Cr goes beyond the scope of this work, we note that the finite- T counterparts of the above two EOSs can be written approximately as $P(\rho, T) = P(\rho) + \alpha T$, where $\alpha_{\text{bcc}} = 7.9 \cdot 10^{-3}$ and $\alpha_{\text{hcp}} = 1.9 \cdot 10^{-2}$. The resulting “approximate” thermal EOSs turn out to be quite accurate. For example, for the six bcc-Cr melting points in Table 1, the corresponding thermal EOS gives pressures of $-5.11, 47.9, 125.1, 265.6, 525.7$ and 815.5 , which are basically identical to those in the third column of Table 1. For the six hcp-Cr melting points in Table 2, the six P values are $1.693, 129.7, 347.2, 691.9, 1094.2$ and 1745.4 , in excellent agreement with those in the fourth column of Table 2.

3.5. Inverse-Z Solidification Simulations of Liquid Cr

To constrain the location of the bcc-hcp solid–solid phase boundary on the P - T plane between the points $(P = 710, T = 0)$ and $(P = 1371, T = 11430)$, we carried out two sets of independent inverse Z runs to solidify liquid Cr and to confirm that liquid Cr solidifies into bcc on one side of this boundary and into hcp (or any other solid structure) on the other side, such that the location of this phase boundary may be constrained.

The inverse Z runs indicate that liquid Cr only solidifies into bcc at ~ 650 GPa in the whole temperature range from 0 to essentially the corresponding T_m . However, at ~ 800 – 1200 GPa it solidifies into bcc above the transition boundary in Figure 6, while below this boundary it solidifies into another solid structure. The radial distribution functions (RDFs) of the final solid states are typical of hexagonal polytypes (red bullets in Figure 6 in the 1200–1400 GPa range), but because they are noisy it is difficult to associate the structure of the final solid state with any of the polytypes (hcp, dhcp, 9R, etc.). To make these RDFs

more discriminating, we fast-quench them to low T . Then, by comparing them to the RDFs of fcc, hcp, dhcp, 9R, etc., we conclude that hcp is the closest structure to those that liquid Cr solidifies into below the transition boundary.

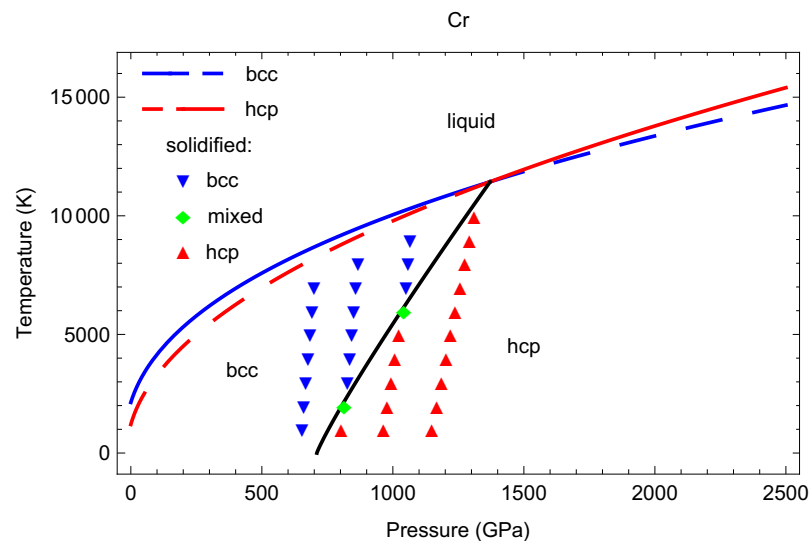


Figure 6. The theoretical phase diagram of Cr based on ab initio quantum molecular dynamics (QMD) simulations.

The RDFs of the solidified states at ~ 1000 GPa above the transition boundary are shown in Figure 7, and of those solidified below the transition boundary in Figure 8. The 6000 K state virtually lies on the boundary. We tentatively assign it to bcc, because it definitely has features of bcc (RDF peaks at $R \sim 50, 60$ and 80 , etc.). At the same time, it certainly has some features that are both uncharacteristic of bcc (e.g., the disappearance of the bcc peaks at $R \sim 115$ and 160 , etc.) and characteristic of hcp (peaks at $R \sim 120, 135, 150$, etc.). Most likely, this 6000 K state is bcc with some admixture of hcp.

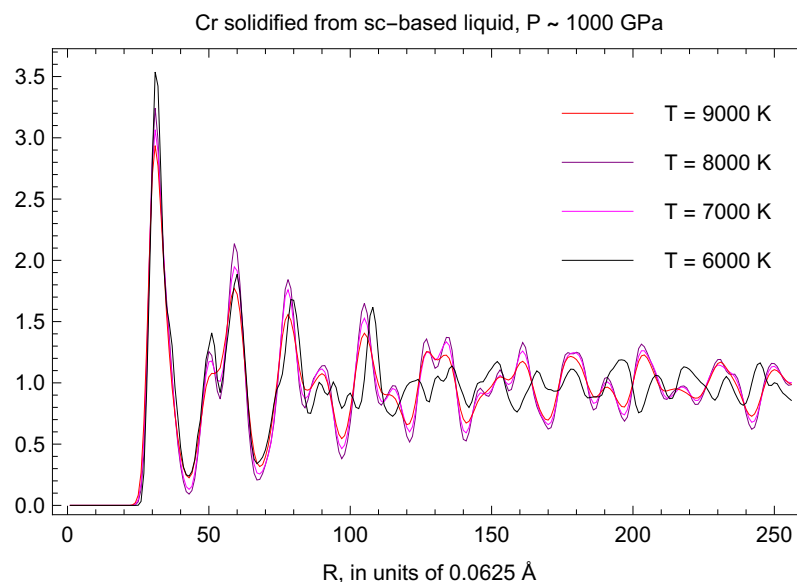


Figure 7. RDFs of the final states of the solidification of liquid Cr at ~ 1000 GPa at higher temperatures.

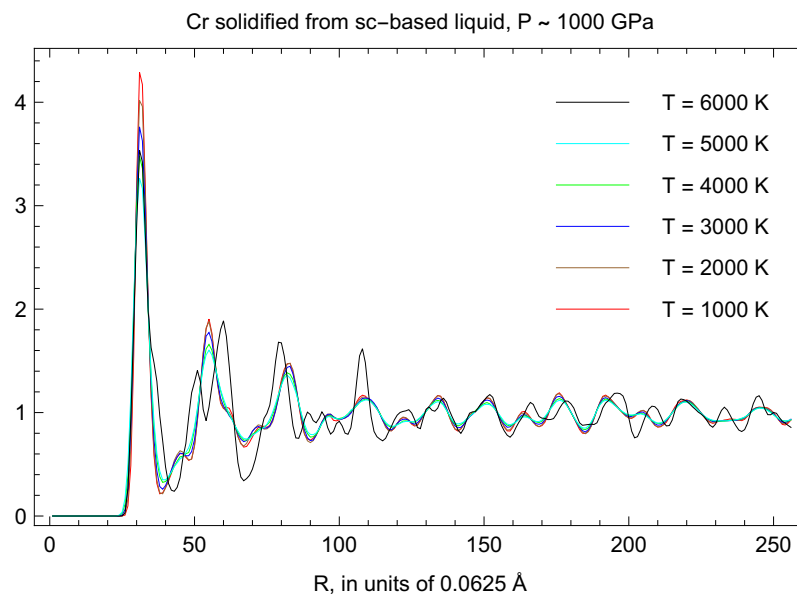


Figure 8. RDFs of the final states of the solidification of liquid Cr at ~ 1000 GPa at lower temperatures.

4. Discussion

The theoretical results described in the previous sections can now be combined into the theoretical phase diagram of chromium. This phase diagram, to 2.5 TPa, is shown in Figure 6. It includes the two, bcc and hcp, melting curves, the bcc-hcp solid–solid phase transition boundary, and the results of the solidification of liquid Cr into final states of either solid bcc or solid hcp, using the inverse Z method.

We note that this is the phase diagram of paramagnetic (nonmagnetic) Cr. The magnetic part takes its very tiny portion in the lower left corner and represents a triangle bounded by $P = 0$, $T = 0$ and $T_N(P)$, which starts at $(P = 0, T = 311 \text{ K})$ and terminates at $(P \sim 20 \text{ GPa}, T = 0)$.

Our theoretical study of the phase diagram of chromium now concludes with a brief discussion of melting on its shock Hugoniot. According to calculations by McQueen et al. ([34], p. 541), the theoretical shock Hugoniot of Cr in the P - T coordinates is given by

$$T_H(P) = 293 + 0.167 P^{1.89}. \quad (6)$$

It crosses the theoretical melting curve of bcc-Cr, Equation (3), at $(P, T) = (244 \text{ GPa}, 5730 \text{ K})$, which is the Hugoniot melting point of Cr. It is consistent with the Hugoniot melting point of V, the nearest neighbor of Cr on the left in PT , namely, $(225 \text{ GPa}, 5690 \text{ K})$ [7], as well as with that of Fe, one of the neighbors of Cr on the right in PT , namely, $(242.5 \pm 19.5 \text{ GPa}, 5600 \pm 850 \text{ K})$ [40]. The Hugoniot melting point of Mn, the nearest neighbor of Cr on the right in PT , is yet to be determined.

The calculated phase diagram of Cr will be useful for geophysics, specifically for modeling the thermal history of the Earth. At pressures corresponding to the Earth's core ($P > 130 \text{ GPa}$), the melting curve of Cr is above the geotherm [41] determined from the PREM model [42]. Thus, at the conditions of the Earth's core, Cr is expected to be solid.

Theoretical ab initio calculations of Ref. [4] and the present work demonstrate that the phase diagrams of the three substances that form Group 6B, i.e., Cr, Mo and W, are topologically similar (look-alike) and have one of the hexagonal polytypes, namely, hcp for Cr and dhcp for both Mo and W, as their high- PT equilibrium solid structure. Additional support for the existence of a hexagonal polytype as a high- PT structure of Group 6B substances comes from Ref. [43]. With decreasing volume (increasing P), the electron wave functions of Cr, Mo and W become more spherically symmetric, which favors a higher atomic coordination number than 8 (of bcc) and therefore a more symmetric structure than bcc. Since the highest possible coordination number is 12 (which comes from the

solution of the famous 3D-sphere-packing problem), corresponding to all of the hexagonal polytypes, namely, hcp (layer stacking sequence AB), fcc (ABC), dhcp (ABAC), triple-hcp (ABCACB), etc., at high P , each of the three Group 6B substances is expected to have one of the hexagonal polytypes as equilibrium solid structure. In contrast to Cr, Mo and W, the study of Ref. [44] shows that the electron wave functions of Group 5B substances V, Nb and Ta behave in exactly the opposite way: with decreasing volume, they become less spherically symmetric, which favors a lower atomic coordination number than bcc's 8, and therefore a less symmetric structure than bcc, e.g., an orthorhombic one. This appears to be in agreement with the fact that, in both Nb [45] and Ta [27], the high- P equilibrium solid structure seems to be an orthorhombic Pnma.

It is interesting to compare the (metastable) ambient melting points of the high- PT hexagonal polytypes of Cr, Mo and W found in ab initio studies to those determined in other theoretical approach. Kaufman and Bernstein [46] estimated the metastable melting points of the hcp and fcc polytypes of Cr, Mo and W by extrapolating enthalpies in their binary phase diagrams to pure hcp and pure fcc. This way, they obtained $T_m(\text{hcp-Cr}) = 1175$ K, $T_m(\text{hcp-Mo}) = 1900$ K and $T_m(\text{hcp-W}) = 2650$ K. The first of the three values is in good agreement with our $T_m(\text{hcp-Cr}) = 1205$ K. Since the values of the metastable T_m of dhcp-Mo and dhcp-W are not estimated in [46], we approximate them by the T_m values for hcp polytypes, taking into account that the corresponding enthalpies are close to each other; see Figure 1 of this work for Cr or Figure 6 of Ref. [4] for W as two examples. Thus, $T_m(\text{dhcp-Mo}) \approx 1900$ K and $T_m(\text{dhcp-W}) \approx 2650$ K, which is in excellent agreement with $T_m(\text{dhcp-Mo}) = 1880$ K and $T_m(\text{dhcp-W}) = 2640$ K from ab initio calculations [4].

5. Conclusions

We have constructed the theoretical phase diagram of chromium to 2.5 TPa, using a suite of ab initio QMD simulations based on the Z methodology which combines both direct Z method for the simulation of melting curves and inverse Z method for the calculation of solid–solid phase boundaries. We determined that hcp-Cr becomes the thermodynamically stable solid structure of chromium at high- PT and finds itself on the phase diagram of chromium, along with bcc-Cr, its solid structure at ambient conditions. We have calculated the melting curves of both bcc-Cr and hcp-Cr, determined the location of the bcc-hcp-liquid triple point, and obtained an equation for the bcc-hcp solid–solid phase transition boundary. Last but not least, we have proposed thermal equations of state for both bcc-Cr and hcp-Cr, which appear to be in good agreement with both experimental data and QMD simulations.

Author Contributions: Methodology, L.B., D.J.L.; software, S.K.S.; investigation, S.R.B., L.B., D.E.; writing—original draft preparation, L.B.; writing—review and editing, D.E.; project administration, D.J.L.; funding acquisition, D.J.L. All authors have read and agreed to the published version of the manuscript.

Funding: This research was carried out under the auspices of the US DOE/NNSA, and was financially supported by the Spanish Ministerio de Ciencia, Innovación y Universidades (Grants Nos. PID2019-106383GB-C41 and RED2018-102612-T), Generalitat Valenciana (Prometeo/2018/123 EFIMAT), and CIPROM/2021/075.

Data Availability Statement: All the data discussed in this work are available from the corresponding author upon request.

Acknowledgments: This research used computational resources provided by the Los Alamos National Laboratory Institutional Computing (IC) Program, which is supported by the U.S. Department of Energy National Nuclear Security Administration under Contract No. 89233218CNA000001. The QMD simulations were performed on the LANL cluster Badger as parts of the IC project w20_phadiagurox.

Conflicts of Interest: The authors declare no conflict of interest.

References

1. Moynier, F.; Yin, Q.-Z.; Schauble, E. Meteoritic Clues Point Chromium Toward Earth's Core. *Science* **2011**, *331*, 1417. [[CrossRef](#)] [[PubMed](#)]
2. Steinitz, M.O.; Schwartz, L.H.; Marcus, J.A.; Fawcett, E.; Reed, W.A. Lattice Anisotropy in Antiferromagnetic Chromium. *Phys. Rev. Lett.* **1969**, *17*, 979. [[CrossRef](#)]
3. Asano, S.; Yamashita, J. Ferromagnetism and Antiferromagnetism in 3d Transition Metals. *Progr. Theor. Phys.* **1973**, *49*, 373. [[CrossRef](#)]
4. Baty, S.R.; Burakovsky, L.; Preston, D.L. Topological Equivalence of the Phase Diagrams of Molybdenum and Tungsten. *Crystals* **2020**, *10*, 20. [[CrossRef](#)]
5. Söderlind, P.; Ahuja, R.; Eriksson, O.; Johansson, B.; Wills, J.M. Theoretical predictions of structural phase transitions in Cr, Mo, and W. *Phys. Rev. B* **1994**, *49*, 9365. [[CrossRef](#)]
6. Errandonea, D.; Schwager, B.; Ditz, R.; Gessmann, C.; Boehler, R.; Ross, M. Systematics of transition-metal melting. *Phys. Rev. B* **2001**, *63*, 132104 [[CrossRef](#)]
7. Errandonea, D.; MacLeod, S.G.; Burakovsky, L.; Santamaria-Perez, D.; Proctor, J.E.; Cynn, H.; Mezouar, M. Melting curve and phase diagram of vanadium under high-pressure and high-temperature conditions. *Phys. Rev. B* **2019**, *100*, 094111 [[CrossRef](#)]
8. Young, D.A. *Phase Diagrams of the Elements*; University of California Press: Berkeley, CA, USA; Los Angeles, CA, USA, 1991; p. 174
9. Lin, R.; Froberg, M.G. Enthalpy measurements of solid and liquid chromium by levitation calorimetry. *High Temp. -High Pres.* **1988**, *20*, 539.
10. Stankus, S.V. Density of vanadium and chromium at high temperatures. *High Temp.* **1993**, *31*, 684.
11. Dubrovinskaya, N.A.; Dubrovinsky, L.S.; Saxena, S.K. Thermal Expansion of Chromium (Cr) to Melting Temperature. *Calphad* **1997**, *21*, 497. [[CrossRef](#)]
12. Gurvich, L.V.; Veits, I.V.; Medvedev, V.A. *Calculations of Thermodynamic Properties*; Nauka: Moscow, Russia, 1982; pp. 9–12.
13. Thurnay, K. *Thermal Properties of Transition Metals, Forschungszentrum Karlsruhe Report FZKA 6095*; INIS: Karlsruhe, Germany, 1998.
14. Anzellini, S.; Errandonea, D.; Burakovsky, L.; Proctor, J.E.; Turnbull, R.; Beavers, C.M. Characterization of the high-pressure and high-temperature phase diagram and equation of state of chromium. *Sci. Rep.* **2022**, *12*, 6727. [[CrossRef](#)] [[PubMed](#)]
15. Blöchl, P. Projector augmented-wave method. *Phys. Rev. B* **1994**, *50*, 17953. [[CrossRef](#)] [[PubMed](#)]
16. Perdew, J.P.; Burke, K.; Ernzerhof, M. Generalized Gradient Approximation Made Simple. *Phys. Rev. Lett.* **1996**, *77*, 3865. [[CrossRef](#)] [[PubMed](#)]
17. Kresse, G.; Hafner, J. Ab initio molecular dynamics for liquid metals. *Phys. Rev. B* **1993**, *47*, 558(R). [[CrossRef](#)]
18. Chen, J.; Singh, D.; Krakauer, H. Local-density description of antiferromagnetic Cr. *Phys. Rev. B* **1988**, *38*, 12834. [[CrossRef](#)]
19. Fawcett, E. Spin-density-wave antiferromagnetism in chromium. *Rev. Mod. Phys.* **1988**, *60*, 209. [[CrossRef](#)]
20. Wang, C.S.; Klein, B.M.; Krakauer, H. Theory of Magnetic and Structural Ordering in Iron. *Phys. Rev. Lett.* **1985**, *54*, 1852. [[CrossRef](#)]
21. Guo, G.Y.; Ebert, H.; Temmerman, W.M.; Schwarz, K.; Blaha, P. Relativistic effects on the structural and magnetic properties of iron. *Solid State Comm.* **1991**, *79*, 121. [[CrossRef](#)]
22. Bagno, P.; Jepsen, O.; Gunnarsson, O. Ground-state properties of third-row elements with nonlocal density functionals. *Phys. Rev. B* **1989**, *40*, 1997(R). [[CrossRef](#)]
23. Barbiellini, B.; Moroni, E.G.; Jarlborg, T. Effects of gradient corrections on electronic structure in metals. *J. Phys. Cond. Mat.* **1990**, *2*, 7597. [[CrossRef](#)]
24. Moroni, E.G.; Kresse, G.; Hafner, J.; Furthmüller, J. Ultrasoft pseudopotentials applied to magnetic Fe, Co, and Ni: From atoms to solids. *Phys. Rev. B* **1997**, *56*, 15629. [[CrossRef](#)]
25. Hobbs, D.; Kresse, G.; Hafner, J. Fully unconstrained noncollinear magnetism within the projector augmented-wave method. *Phys. Rev. B* **2000**, *62*, 11556. [[CrossRef](#)]
26. Belonoshko, A.B.; Skorodumova, N.V.; Rosengren, A.; Johansson, B. Melting and critical superheating. *Phys. Rev. B* **2006**, *73*, 012201. [[CrossRef](#)]
27. Burakovsky, L.; Chen, S.P.; Preston, D.L.; Sheppard, D.G. Z methodology for phase diagram studies: platinum and tantalum as examples. *J. Phys. Conf. Ser.* **2014**, *500*, 162001. [[CrossRef](#)]
28. Burakovsky, L.; Burakovsky, N.; Preston, D. Ab initio melting curve of osmium. *Phys. Rev. B* **2015**, *92*, 174105. [[CrossRef](#)]
29. Dubrovinskaya, N.; Dubrovinsky, L.; Solopova, N.A.; Abakumov, A.; Turner, S.; Hanfl, M.; Bykova, E.; Bykov, M.; Prescher, C.; Prakapenka, V.B.; et al. Terapascal static pressure generation with ultrahigh yield strength nanodiamond. *Sci. Adv.* **2016**, *2*, 1600341. [[CrossRef](#)]
30. White, G.K.; Smith, T.F.; Carr, R.H. Thermal expansion of Cr, Mo and W at low temperatures. *Cryogenics* **1978**, *18*, 301. [[CrossRef](#)]
31. Guo, G.Y.; Wang, H.H. Calculated elastic constants and electronic and magnetic properties of bcc, fcc, and hcp Cr crystals and thin films. *Phys. Rev. B* **2000**, *62*, 5136. [[CrossRef](#)]
32. Skriver, H.L. The electronic structure of antiferromagnetic chromium. *J. Phys. F* **1981**, *11*, 97. [[CrossRef](#)]
33. Jaramillo, R.; Feng, Y.; Lang, J.C.; Islam, Z.; Srajer, G.; Littlewood, P.B.; McWhan, D.B.; Rosenbaum, T.F. Breakdown of the Bardeen-Cooper-Schrieffer ground state at a quantum phase transition. *Nature* **2009**, *459*, 405. [[CrossRef](#)]
34. McQueen, R.G.; Marsh, S.P.; Taylor, J.W.; Fritz, J.N.; Carter, W.J. *High-Velocity Impact Phenomena, Chap. VII—The Equation of State of Solids from Shock Wave Studies*; Academic Press: New York, NY, USA; London, UK, 1970.

35. Abrikosov, I.; Ponomareva, A.; Steneteg, P.; Barannikova, S.; Alling, B. Recent progress in simulations of the paramagnetic state of magnetic materials. *Curr. Opin. Sol. State Mat. Sci.* **2016**, *20*, 85. [[CrossRef](#)]
36. Dudarev, S.L.; Botton, G.A.; Savrasov, S.Y.; Humphreys, C.J.; Sutton, A.P. Electron-energy-loss spectra and the structural stability of nickel oxide: An LSDA+U study. *Phys. Rev. B* **1998**, *57*, 1505. [[CrossRef](#)]
37. Aryasetiawan, F.; Karlson, K.; Jepsen, O.; Schönberger, U. Calculations of Hubbard U from first-principles. *Phys. Rev. B* **2006**, *74*, 125106. [[CrossRef](#)]
38. Makeev, V.V.; Popel, P.S. Density and coefficients of thermal expansion of nickel, chromium, and scandium in the solid and liquid states. *High Temp.* **1990**, *28*, 525.
39. Górecki, T. Vacancies and a generalised melting curve of metals. *High Temp.-High Pres.* **1979**, *11*, 683.
40. Nguyen, J.H.; Holmes, N.C. Melting of iron at the physical conditions of the Earth's core. *Nature* **2004**, *427*, 339. [[CrossRef](#)]
41. Available online: <https://www.geo.arizona.edu/xtal/geos306/geotherm.htm> (accessed on 1 June 2022).
42. Dziewonski, A.M.; Anderson, D.L. Preliminary reference Earth model. *Phys. Earth Planet. Inter.* **1981**, *25*, 297. [[CrossRef](#)]
43. Xie, Y.-Q.; Deng, Y.-P.; Liu, X.-B. Electronic structure and physical properties of pure Cr, Mo and W. *Trans. Nonferrous Met. Soc. China* **2003**, *13*, 5.
44. He, Y.; Xie, Y.-Q. Electronic structure and properties of V, Nb and Ta metals. *J. Cent. South Univ. Technol.* **2000**, *7*, 7. [[CrossRef](#)]
45. Errandonea, D.; Burakovsky, L.; Preston, D.L.; MacLeod, S.G.; Santamaría-Perez, D.; Chen, S.; Cynn, H.; Simak, S.I.; McMahon, M.I.; Proctor, J.E. Experimental and theoretical confirmation of an orthorhombic phase transition in niobium at high pressure and temperature. *Comms. Mater.* **2020**, *1*, 60. [[CrossRef](#)]
46. Kaufman, L.; Bernstein, H. *Computer Calculation of Phase Diagrams with Special Reference to Refractory Metals*; Academic Press: New York, NY, USA; London, UK, 1970; Volume 25, p. 297.